Detection of small internal fatigue cracks in Ti-6Al-4V via synchrotron radiation nanocomputed tomography

Gaoge Xue[1], Yuta Tomoda[1], Takashi Nakamura[2*], Nao Fujimura[2], Kosuke Takahashi[2], Fumiyoshi Yoshinaka[3], Akihisa Takeuchi[4], Masayuki Uesugi[4] and Kentaro Uesugi[4]

[1]*Division of Mechanical and Space Engineering, Hokkaido University, Japan*

[2]*Division of Mechanical and Aerospace Engineering, Hokkaido University, Japan*

[3]*National Institute for Materials Science (NIMS), Japan*

[4]*Japan Synchrotron Radiation Research Institute (JASRI), SPring-8, Japan*

*Corresponding author: nakamut@eng.hokudai.ac.jp

Abstract

Two types of synchrotron radiation computed tomography (SR-CT)—projection CT (micro-CT) and phase-contrast imaging CT (nano-CT)—were used to observe internal fatigue cracks in (α+β) Ti-6Al-4V alloy. Micro-CT detected cracks in the specimen at ~1 μm spatial resolution, and the nano-CT provided magnified images at ~200 nm spatial resolution. The crack initiation sites were clarified as the α−phase for both the surface and internal cracks; however, their opening behaviors differed. A sharp crack tip was observed in the surface crack, and the crack tip opening displacement (CTOD) increased with an increase in the applied load. By contrast, a blunted crack tip, similar to that of a crack in a vacuum, was observed for the internal crack, and its CTOD remained almost constant regardless of the applied load. These phenomena are likely to explain the different behaviors of surface and internal cracks, particularly the slower growth rate of internal cracks, which leads to a longer fatigue life in the very high cycle fatigue regime.

1 Introduction

Ti-6Al-4V has many attractive properties, including high specific strength, superior heat resistance, and remarkable corrosion resistance. In particular, its excellent fatigue properties make it suitable for use in mechanical components subject to severe cyclic loading. However, in the very high cycle fatigue (VHCF) regime, fracture occurs from the initiation and propagation of small cracks starting from inside the material[1–6]. The mechanism of this phenomenon remains unknown because the initiation site size is approximately 10 μm, and thus too small to be detected by commonly used X-ray computed tomography (CT). The difficulties involved in performing nondestructive observations of small internal cracks have become a bottleneck in the study of the VHCF of this alloy.

In recent years, synchrotron radiation CT (SR-CT) has gained increasing attention as a novel nondestructive inspection (NDI) technique in the field of material strength and failure analysis[7]. This technique has also been utilized in fatigue research to investigate crack behavior in metallic materials[8–14]. In particular, third-generation synchrotron radiation facilities equipped with insertion devices, such as ESRF in France, APS in the US, and SPring-8 in Japan, can provide high-brightness synchrotron radiation of very high intensity, which makes it possible to carry out an NDI with a high spatial resolution of 1 μm or less. This excellent ability makes it possible to detect internal defects and observe small fatigue cracks nondestructively. For instance, Serrano-Munoz et al. studied the influence of casting defects on the fatigue crack initiation in A357 Al alloy[8]. Messager et al. conducted *in-situ* ultrasonic fatigue tests along with microtomography, and captured the internal crack initiation from an artificial casting defect in A357 Al alloy[9]. Tubei et al. investigated the three-dimensional closure behavior of small cracks in Ti-6Al-4V[11].

In addition to these attempts, our team has also applied SR-CT (as provided by the SPring-8 facility) to detect internal cracks in (α+β) Ti-6Al-4V[15–17]. In our previous study, we succeeded in observing small internal cracks by employing a projection CT (micro-CT) and found that the internal crack propagated at an extremely slow rate (between 10^{-13} to 10^{-11} m/cycle). However, the details of the initiation and propagation processes of the internal cracks are not yet fully understood owing to the insufficient resolution of the crack images. Therefore, we herein introduced phase-contrast imaging CT with a high spatial resolution in a nano meter order, referred to as nano-CT[18,19]. The nano-CT enabled the visualization of microstructure. Liu et al. used nano-CT to investigate the three-dimensional microstructures of the fine granular area in high strength steel[20]. Additionally, we successfully observed the mutual interaction between a small surface crack with the local microstructure by nano-CT in a beta titanium alloy Ti-22V-4Al[21]. Therefore, it is

expected that clearer images of small internal cracks than those of micro-CT with the surrounding microstructure could be obtained. In this work, the difference between the opening behavior of small internal cracks and that of surface cracks was compared, and the possible reasons for the slow growth of internal cracks were discussed.

2 Experimental procedure

2.1 Material and specimen

The material used was the (α+β)-type Ti-6Al-4V alloy provided by Daido Steel Co., Ltd., Japan. The chemical composition of the material was Al: 6.12, V: 4.27, O: 0.16, N: 0.002, C: 0.02, Fe: 0.15, and H: 0.0029, and the balance wt% as Ti. First, the ϕ 780 mm ingots were forged into ϕ 440 mm bars and then gyratory forged into ϕ 20 mm bars for preparing the specimens. The ϕ 20 mm bars were heat-treated with a solution treatment at 1203 K for 3.6 ks, followed by air cooling and then aging at 978 K for 7.2 ks. Fig. 1 shows a scanning electron microscope (SEM) image of the microstructure after heat treatment. The SEM image shows a two-phase microstructure with equiaxed alpha grains and grains containing alternating lamellae of alpha and beta phases. The average size of both types is approximately 10 μm. Three tensile tests were conducted following ISO 6892-1 standard series using ϕ 4 mm specimens, and the following mechanical properties were obtained: tensile strength of 943 MPa, 0.2 % proof stress of 860 MPa, elongation to failure of 17 %, area reduction of 40 %, and Vickers hardness of 316 HV.

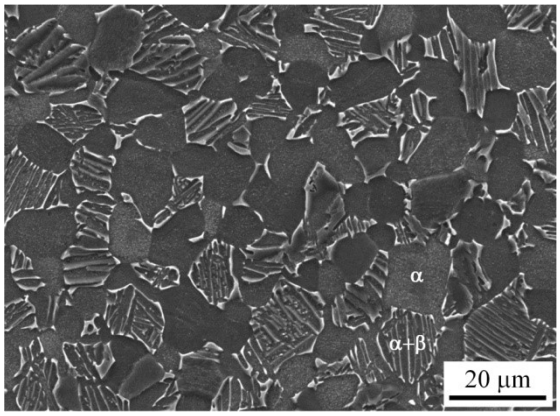

Fig. 1 SEM image of the microstructure of the applied (α+β) titanium alloy Ti-6Al-4V, consisting of a two-phase microstructure with equiaxed alpha grains and grains containing alternating lamellae of alpha and beta phases.

Fig. 2 shows an internal crack observed through micro-CT using an hourglass-shaped specimens with a straight section of ϕ 1.8 mm × 3 mm in our previous study[15,16]. A small crack was recognized in the figure; however, the image quality was not sufficient. To increase the X-ray transmittance for a clearer image of the crack, we prepared a thinner specimen with a diameter of 0.8 mm, as shown in Fig. 3. The specimens were lathe-turned from the above-mentioned round bars. The surface was finished using #120 to #2000 grit emery paper with a depth of approximately 50 μm to eliminate the work-hardened layer; hence, we finally reached a control volume part with ϕ 0.7 mm × 3 mm. The X-ray transmittance at the control volume of this specimen at 30 keV was 21%.

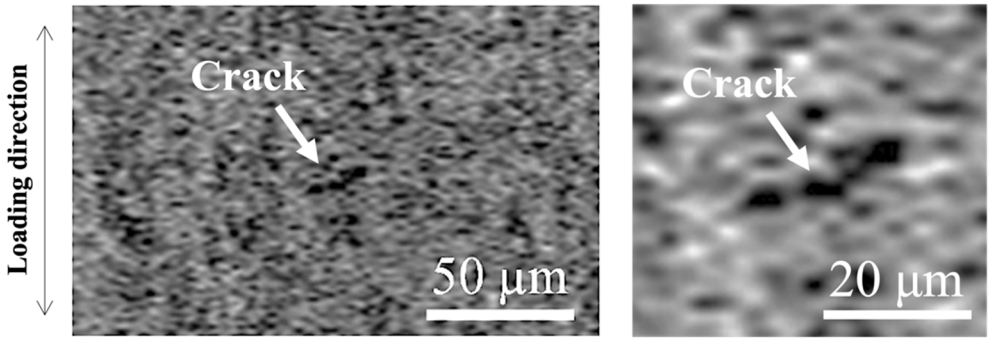

Fig. 2 Micro-CT image of an internal crack by using ϕ 1.8 mm specimen[16]; (a) shows the low magnification image and (b) shows the high magnification image. Tensile loading corresponding to 78% of the maximum stress was applied during CT observation; the fatigue loading number was 5×10^6 at σ_{max} = 650 MPa under R = 0.1

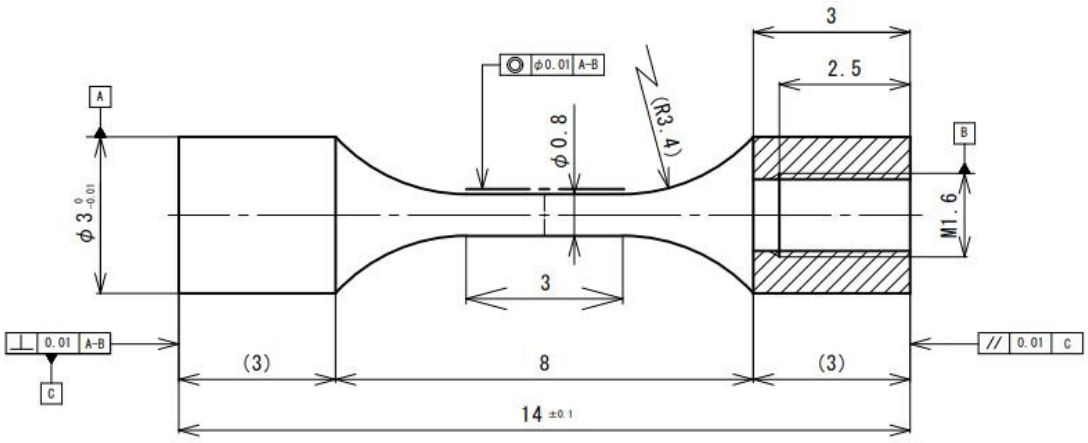

Fig. 3 Specimen configuration (unit: mm).

2.2 Condition of fatigue tests

The basic fatigue properties were examined using a hydraulic servo fatigue testing machine prior to the CT observation. Fig. 4 shows an *S–N* diagram of the ϕ 0.7 mm specimens used in this study with the data from ϕ 1.8 mm specimens under R = 0.1[15,16]. The fatigue data were distinguished based on the position at which the crack was initiated. The circles in Fig. 4 indicate the surface fracture, the triangles indicate the internal fracture, and the diamonds indicate the combined fracture, which corresponds to the data obtained from the fracture by the coalescence of internal and surface cracks[4]. No significant difference was observed between the fatigue data of the ϕ 0.7 mm and ϕ 1.8 mm specimens. Based on the *S–N* diagram, σ_{max} = 650 MPa was determined as the maximum stress used in the CT experiments to obtain internal fractures at a relatively small number of cycles while avoiding the surface fracture. In this study, the CT observations were made at $N = 4.0 \times 10^6$ and 4.2×10^6 cycles. The fatigue test frequency for CT imaging was set at 140 Hz.

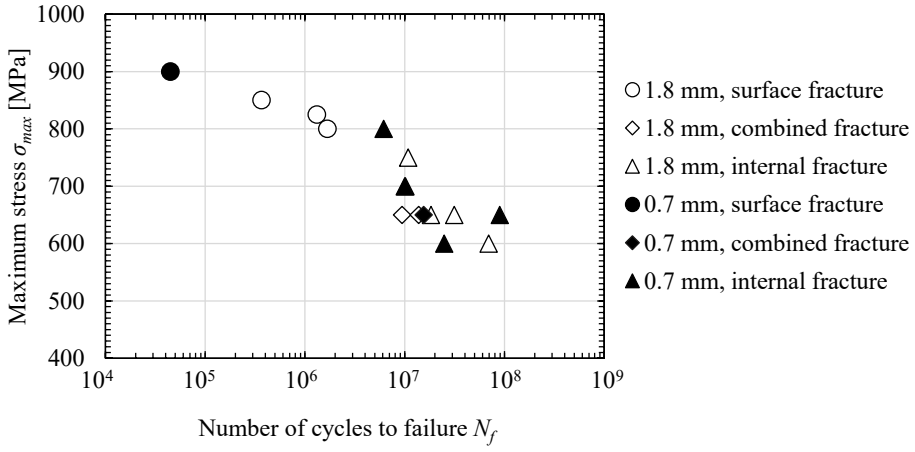

Fig. 4 *S–N* diagram under the condition of R = 0.1 and test frequency of 120–250 Hz. Maximum stress of 650 MPa under 140 Hz was applied to the specimen in the experiments performed at SPring–8.

2.3 Experimental setup and imaging conditions

SR-CT was conducted at beamline BL20XU at SPring-8. This beamline offers two different types of CT: a projection CT (micro-CT) and a phase-contrast imaging CT (nano-CT)[22,23]. The two CTs can be switched at any time. Fig. 5 shows an outline of the experimental setup for CT. In both systems, radiation from the light source (hybrid-type in-vacuum undulator) was diffracted by a double crystal monochromator (Si 111-111), and the specimen was irradiated with monochromatic X-rays. The spatial resolution of micro-CT was approximately 1 μm[18,24]. The nano-CT utilizes the

phase shift of the X-rays, enabling more sensitive imaging. A Fresnel zone plate was used as an objective X-ray lens to magnify the observed image, and a Zernike phase plate was employed to convert the phase shift into the intensity. The spatial resolution of the nano-CT was ~200 nm[19]. More details including their achieved spatial resolution are described elsewhere[18,19,24]. Micro-CT was used to detect the internal cracks in the specimen, and nano-CT was used to observe the crack shape, the opening behaviors, and their relationship with the surrounding microstructure. During the observation, the specimen was set in a loading fixture (see Fig. 6). For micro-CT, no tensile load was applied during imaging. In the case of nano-CT, various tensile loads were applied to observe the crack opening behaviors (details in section 3.2). In both CTs, the X-ray energy was 30.0 keV, and the specimen was rotated about the longitudinal axis from 0° to 180° in steps of 0.1°. At each step, the X-ray intensity was measured with an exposure time of 0.5 s for the micro-CT and 1.0 s for the nano-CT. The CT imaging conditions are presented in Table 1. The voxel sizes for micro-CT and nano-CT were 0.51 and 0.0654 μm, respectively.

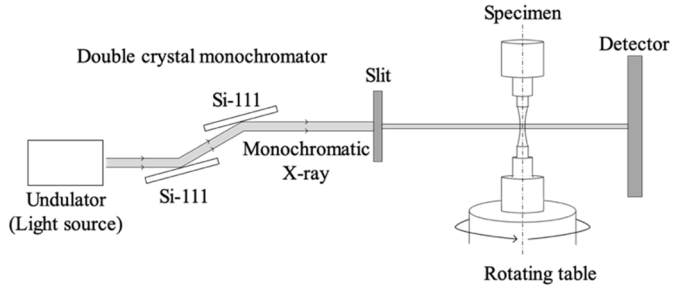

(a) Projection computed tomography (micro-CT)

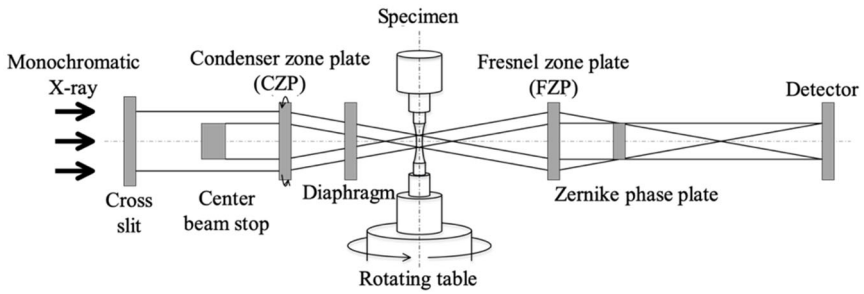

(b) Phase contrast imaging computed tomography (nano-CT)

Fig. 5 Observation system of BL20XU at SPring–8; (a) shows the projection CT and (b) shows the phase-contrast imaging CT.

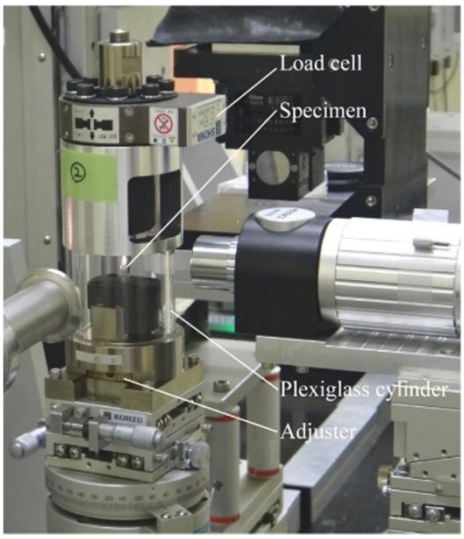

Fig. 6 Loading fixture setup during imaging[15,16].

Table 1 Conditions of CT imaging

CT Type	X-ray energy (keV)	Sample-detector distance (m)	Projection number	Field of view (mm × mm)	Voxel size (μm)
Projection CT (micro-CT)	30.0	0.03	1800	1.0 × 1.0	0.51
Phase-contrast imaging CT (nano-CT)		165*		0.057 × 0.057	0.0654

* This value is for reference purposes only.

3 Results

3.1 Results of Micro-CT

Observation using micro-CT at $N = 4.0 \times 10^6$ cycles revealed that one surface crack and six internal cracks had already initiated in the specimen. Then, at $N = 4.2 \times 10^6$ cycles, another surface crack initiated, which indicates that the initiation of internal cracks could occur earlier than that of surface cracks. The positions of the cracks are schematically illustrated in Fig. 7, which shows the cracks were distributed roughly evenly, and no densely initiated regions were observed in the examined volume. Then, the cracks were sliced along the line of the largest gradient for the cross-sectional views as shown in Fig. 8, and the horizontal distance between two crack tips was defined as the crack length. The cracks are arranged in numerical order of the crack length (from longest), and the “S-2” is the latest initiated surface crack. The crack length of the surface cracks were 15.6

μm and 7.6 μm. The maximum, minimum, and average crack length for the internal cracks were 9.3 μm, 6.3 μm, and 7.8 μm, respectively. These values were comparable to or slightly smaller than the average grain size.

Regarding the image quality, the small crack can be recognized more easily and clearly in the ϕ 0.7 mm specimen than in the ϕ 1.8 mm specimen (see Fig. 2). Nevertheless, the resolution of the crack images by micro-CT was still insufficient to measure the opening behavior and clarify the relationship between the crack and the surrounding microstructure.

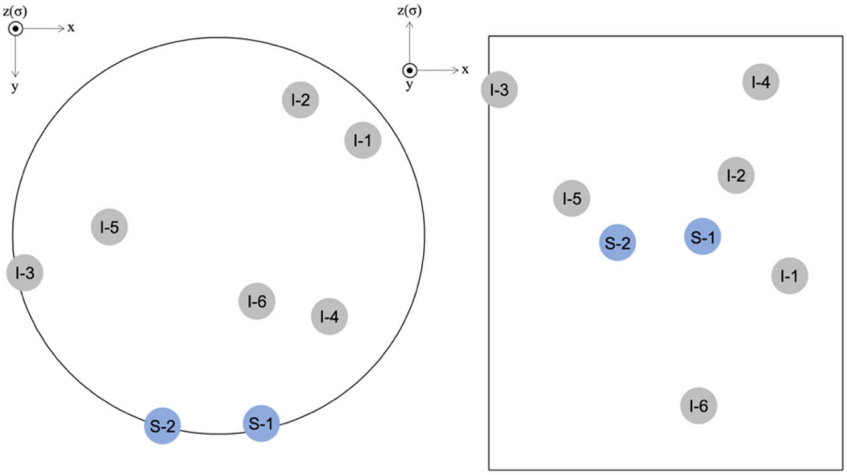

Fig. 7 Crack initiation sites in the observation region. z(σ) is the longitudinal direction of the specimen; the cracks are numbered in order of the crack length (from longest).

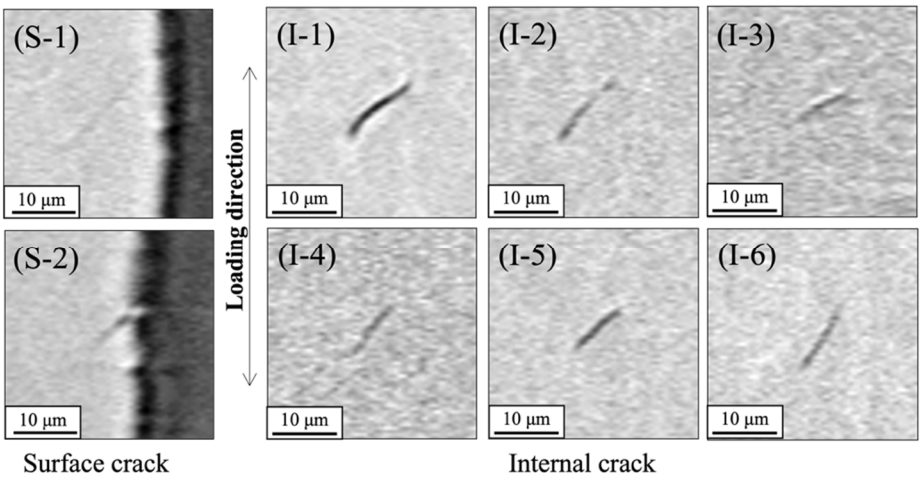

Fig. 8 Small fatigue cracks detected by the projection type CT (micro-CT). (S-1) and (S-2) show the surface cracks; (I-1) ~ (I-6) show the internal cracks.

3.2 Results of nano-CT

To obtain a clearer image and the opening behavior of the small cracks, we applied nano-CT at $N = 4.2 \times 10^6$ cycles to the surface crack (S-1) and two internal cracks (I-1) and (I-6) in Fig. 8. All three cracks were imaged under a tensile load equivalent to the maximum fatigue test stress (σ/σ_{max} = 100%) and the no-loading condition (σ/σ_{max} = 0%). Additionally, 10%, 20%, 30%, 40%, 60%, and 80% loading conditions were applied for the surface crack (S-1) and internal crack (I-1).

As an example, the 3D images of surface crack (S-1) and internal crack (I-1) are shown in Fig. 9. Similar to the micro-CT images, the cracks were sliced along the largest gradient, which are shown by the black dashed lines. Fig. 10 shows the sectional views of the cracks under various tensile loads by nano-CT. The shapes and sizes of the cracks were much more clearly observed with nano-CT than with micro-CT. In addition, the α- and β-phases, which cannot be distinguished in Fig. 8, were also identified. Both surface and internal cracks were initiated in the α-phase and inclined at 36°–55° from the loading direction. This suggests that the slip in the α-phase could be the reason for crack initiation, regardless of whether the crack is initiated at the surface or internal region.

The crack tips are highlighted using white arrows in Fig. 10. The surface crack reached the adjacent β-grain ((α+β) phase); similarly, both tips of the internal cracks also reached the β-grain. These results suggest that β-grains resist the subsequent growth of a crack initiated in the α-phase for both surface and internal cracks.

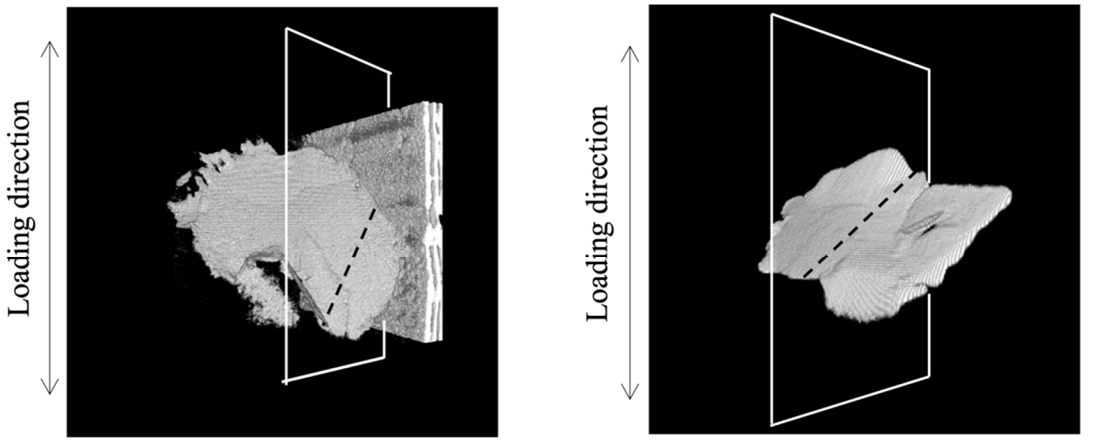

(a) 3D images of the surface crack (S-1) (b) 3D images of the internal crack (I-1)

Fig. 9 3D images built using nano-CT. Black dashed line represents the image slice location.

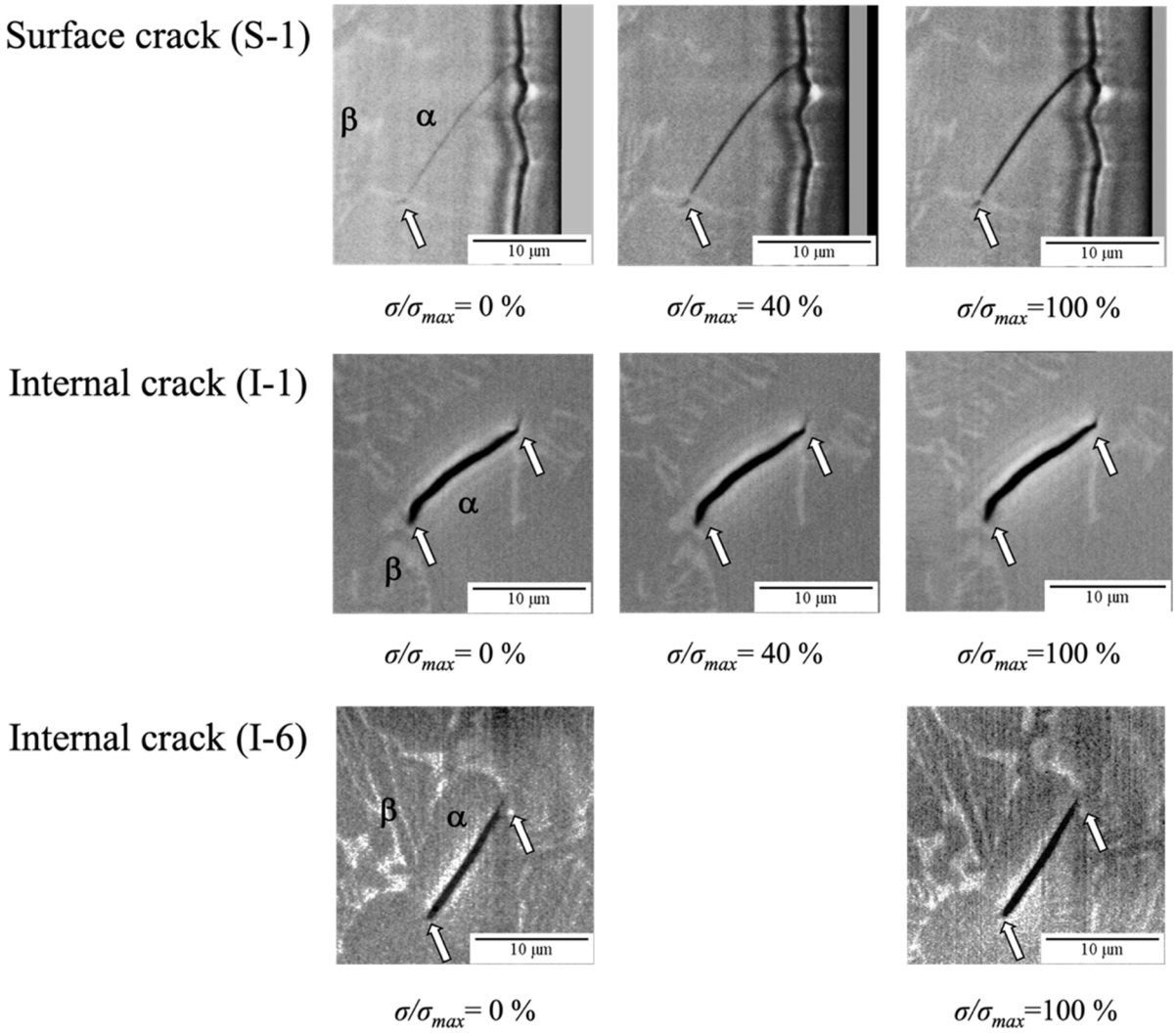

Fig. 10 Crack opening behavior observed using the phase-contrast imaging CT (nano-CT). White arrows show the crack tips.

A clear difference between the surface and internal cracks was observed, focusing on the crack shape and opening behavior. The tip of the surface crack was very sharp, and the crack gradually opened with increasing applied load. By contrast, both tips of the internal cracks were blunted, and the opening displacement near the crack tip of the internal crack was larger than that of the surface crack. The internal crack likely remained unchanged with respect to the applied load. To confirm the tendencies quantitatively, we measured the crack opening displacement at 0.5 μm behind the crack tip for one surface crack (S-1) and two internal cracks (I-1 and I-6); this measurement was repeated six times for each crack tip. The averaged value from both crack tips was regarded as the CTOD of the internal crack, and that from a single crack tip was regarded as the CTOD of the surface crack. The standard deviation of each plotted CTOD for the surface crack (S-1) was less than 0.029 μm, while those for the internal cracks (I-1 and I-6) were less than 0.051

and 0.045 μm, respectively. Fig. 11 shows the relationship between the CTOD and the applied load of the cracks. The CTOD of the internal cracks were larger than that of the surface crack, although the crack lengths were similar. In addition, the CTOD of the surface crack gradually increased with increasing load, and remained consistent after 40% tensile stress; however, that of the internal cracks remained almost constant, regardless of the applied stress.

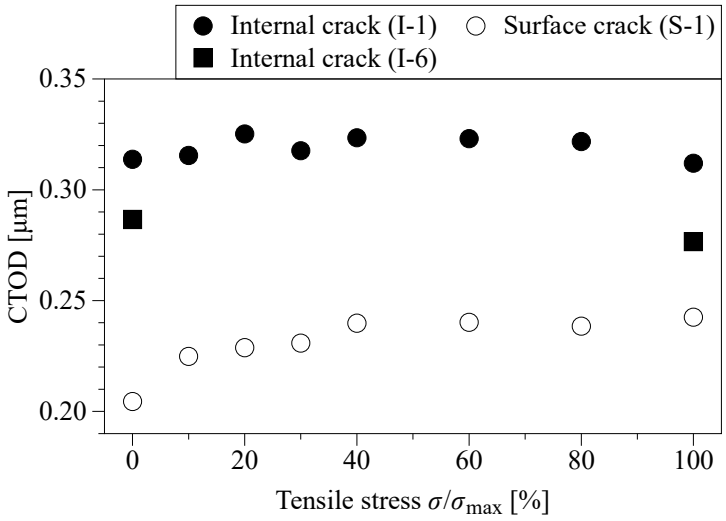

Fig. 11 Comparison between crack tip opening displacement (CTOD) of the surface crack and internal cracks under various tensile loadings.

4 Discussion

Previous studies on Ti-6Al-4V indicated that internal cracks are similar to the cracks in a vacuum in terms of fractography and crack propagation rate[25,26]. The fracture surface topography exhibited a granular feature with rounded edges in both the internal cracks and cracks in a vacuum. Meanwhile, the crack propagation rate of internal cracks was plotted in the range of 10^{-13} to 10^{-11} m/cycle, which is in good agreement with that of the cracks in a vacuum. In this study, we obtained the CTOD behavior of the internal crack; therefore, the similarity of CTOD between the internal cracks and cracks in a vacuum is worth discussing in this section.

Researchers have studied crack tip behavior in air and vacuum for various metallic materials. For example, Wanhill[27] found that crack blunting occurred in a vacuum for aluminum alloys 2024-T3 and 7075-T6; McEvily et al. reported a blunter shape of the fatigue crack tip and a larger CTOD in a vacuum than those in air for stainless steels 304 and 316, and aluminum alloy 2219[28]. In addition, Gach et al. pointed out that the crack tip opening angle was greater in vacuum than in air for an austenitic stainless steel and aluminum alloy 7020[29]. Although the material used in this study,

Ti-6Al-4V, is different from the above, the dissimilarities of crack tip behaviors between vacuum and air were identical to those of the internal and surface cracks in this study. This agreement provides further evidence that the internal crack in Ti-6Al-4V is comparable to a crack in vacuum. Based on the above findings, the blunter behavior of the internal fatigue crack tip can be explained by the easier plastic deformation in a vacuum[30,31]. Meanwhile, because of the absence of strain localization due to the shortage of oxygen[32], water vapor[33], and hydrogen[34], the occurrence of embrittlement fracture (which contributes to a sharp crack) is hardly favored in a vacuum.

Regarding the CTOD tendency in Fig. 11, the CTOD of internal cracks remain constant regardless of the applied stress; similarly, the CTOD of surface cracks were also found to be consistent after 40% of the applied stress. Morris reported that the grain boundary could confine the plastic deformation in a small crack regime so that the CTOD could become insensitive to the external tensile load[35]. In this study, both the surface and internal crack tips in Fig. 10 reached the grain boundary, which might be another factor, in addition to the rounded crack tip, contributing to the constant CTOD of cracks in a grain-size order. Conversely, considering that ΔCTOD (i.e., the CTOD ranges from no-stress to maximum tensile stress) corresponds to the driving force for crack growth, a small ΔCTOD of internal cracks indicates that internal cracks initiated in the α-phase cannot easily propagate as compared to the surface cracks. The crack opening behaviors could differ in terms of several factors including the crack orientation, distance from the crack tip, and the local microstructure. Thus, although further investigations are required to fully understand the internal crack behavior, the above finding does not contradict the longer fatigue life of internal fractures.

5 Conclusion

Two types of SR-CT—micro-CT and nano-CT—were employed to detect internal fatigue cracks in Ti-6Al-4V alloy. Micro-CT detected cracks in the specimen, while nano-CT provided high-resolution magnified images. The main findings are as follows.

1. Both surface and internal cracks initiated in the α-phase, and both types of cracks were inclined at 36°–55° from the loading direction. This suggests that slippage in the α-phase can be the reason for crack initiation, regardless of the type of crack.
2. The surface cracks exhibited sharp crack tips, and their CTODs were sensitive to the applied load. By contrast, the internal cracks had a blunt crack tip, which was similar to the shape of the fatigue crack in a vacuum. The CTODs of the internal cracks were larger than those of the

surface cracks and remained almost constant, regardless of the applied load. These findings do not contradict the fact that internal cracks in the VHCF regime have longer lives than surface cracks.

Acknowledgment

We would like to express our sincere gratitude to Daido Steel Co., Ltd. for providing the experimental material. The synchrotron radiation experiments were performed at the BL20XU of SPring-8, Japan, with the approval of the Japan Synchrotron Radiation Research Institute (JASRI; Proposal No. 2017B1421 and 2018B1289). This research was funded by the Japan Society for the Promotion of Science (JSPS) in Japan (grant numbers: Scientific Research (A, 18H03748 and 21H04529). It was also supported by the F3 Engineering Education and Research Center at the Faculty of Engineering, Hokkaido University, and the Ambitious Doctoral Fellowship from Hokkaido University. We would like to thank Editage for English language editing.

Conflict of Interests

The authors declare no conflict of interest.

Author Contribution

The authors confirm contributions to the paper as below: Conceptualization and manuscript preparation: Gaoge Xue and Yuta Tomoda; Experiments and data analysis: Gaoge Xue, Yuta Tomoda. and Nao Fujimura; Review and editing: Takashi Nakamura, Kosuke Takahashi, Fumiyoshi Yoshinaka and Akihisa Takeuchi; Resources: Akihisa Takeuchi, Masayuki Uesugi and Kentaro Uesugi; Funding acquisition: Takashi Nakamura. All authors have read and agreed to the published version of the manuscript.

Data Availability

The data that support the findings of this study are available from the corresponding author upon reasonable request.

References:

1 Neal DF, Blenkinsop PA. Internal fatigue origins in α-β titanium allols. *Acta Metall*. 1976;24: 59–63.

2 Atrens A, Hoffelner W, Duerig TW, Allison JE. Subsurface crack initiation in high cycle fatigue in Ti6A14V and in a typical martensitic stainless steel. *Scr Metall*. 1983;17: 601–606.

3 Nalla R, Boyce B, Campbell J, Peters J, Ritchie R. Influence of microstructure on high-cycle fatigue of Ti-6Al-4V: Bimodal vs. lamellar structures. *Metall Mater Trans A Phys Metall Mater Sci*. 2002;33: 899–918.

4 Oguma H, Nakamura T. The effect of microstructure on very high cycle fatigue properties in Ti–6Al–4V. *Scr Mater*. 2010;63: 32–34.

5 Heinz S, Balle F, Wagner G, Eifler D. Analysis of fatigue properties and failure mechanisms of Ti6Al4V in the very high cycle fatigue regime using ultrasonic technology and 3D laser scanning vibrometry. *Ultrasonics*. 2013;53: 1433–1440.

6 Liu X, Sun C, Hong Y. Effects of stress ratio on high-cycle and very-high-cycle fatigue behavior of a Ti-6Al-4V alloy. *Mater Sci Eng A*. 2015;622: 228–235.

7 Wu S, Xiao T, Withers PJ. The imaging of failure in structural materials by synchrotron radiation X-ray microtomography. *Eng Fract Mech*. 2017;182: 127–156.

8 Serrano-Munoz I, Buffiere JY, Verdu C. Casting defects in structural components: Are they all dangerous? A 3D study. *Int J Fatigue*. 2018;117: 471–484.

9 Messager A, Junet A, Palin-Luc T, et al. In situ synchrotron ultrasonic fatigue testing device for 3D characterisation of internal crack initiation and growth. *Fatigue Fract Eng Mater Struct*. 2020;43: 558–567.

10 Zhang H, Toda H, Hara H, et al. Three-dimensional visualization of the interaction between fatigue crack and micropores in an aluminum alloy using synchrotron X-ray microtomography. *Metall Mater Trans A Phys Metall Mater Sci*. 2007;38: 1774–1785.

11 Tubei V, Toda H, Hassanipour M, et al. 3D short fatigue crack closure behavior in Ti-6Al-4V alloy investigated using in-situ high resolution synchrotron X-ray tomography. *Eng Fract Mech*. 2021;249: 107755.

12 Qian W, Wu S, Wu Z, et al. In situ X-ray imaging of fatigue crack growth from multiple defects in additively manufactured AlSi10Mg alloy. *Int J Fatigue*. 2022;155: 106616.

13 King A, Ludwig W, Herbig M, et al. Three-dimensional in situ observations of short fatigue crack growth in magnesium. *Acta Mater*. 2011;59: 6761–6771.

14 Birosca S, Buffiere JY, Karadge M, Preuss M. 3-D observations of short fatigue crack interaction with lamellar and duplex microstructures in a two-phase titanium alloy. *Acta Mater*. 2011;59: 1510–1522.

15 Yoshinaka F, Nakamura T, Nakayama S, Shiozawa D, Nakai Y, Uesugi K. Non-destructive observation of internal fatigue crack growth in Ti–6Al–4V by using synchrotron radiation μCT imaging. *Int J Fatigue*. 2016;93: 397–405.

16 Yoshinaka F, Nakamura T, Takeuchi A, Uesugi M, Uesugi K. Initiation and growth behaviour of small internal fatigue cracks in Ti-6Al-4V via synchrotron radiation microcomputed tomography. *Fatigue Fract Eng Mater Struct*. 2019;42: 2093–2105.

17 Nakamura T, Yoshinaka F, Nakayama S, et al. Detection of small internal fatigue cracks in Ti-6Al-4V by using synchrotron radiation μCT imaging. *Mech Eng Lett*. 2016;2: 16-00233-16–00233.

18 Takeuchi A, Suzuki Y. Recent progress in synchrotron radiation 3D-4D nano-imaging based on X-ray full-field microscopy. *Microscopy*. 2020;69: 259–279.

19 Takeuchi A, Uesugi K, Uesugi M, et al. High-energy X-ray nanotomography introducing an apodization Fresnel zone plate objective lens. *Rev Sci Instrum*. 2021;92: 023701.

20 Liu L, Hou N, Li B, Ma B, Hu S, Ding N. Structure characterization within the vicinity of the fine granular area by synchrotron radiation nano-CT. *Fatigue Fract Eng Mater Struct*. 2020;43: 1597–1605.

21 Xue G, Nakamura T, Fujimura N, et al. Initiation and propagation of small fatigue crack in beta titanium alloy observed through synchrotron radiation multiscale computed tomography. *Eng Fract Mech*. 2022;263: 108308.

22 Suzuki Y, Uesugi K, Takimoto N, et al. Construction and commissioning of A 248 m-long beamline with X-ray undulator light source. In: *AIP Conference Proceedings*. Vol 705. American Institute of PhysicsAIP; 2004:344–347.

23 Takeuchi A, Uesugi K, Uesugi M, Yoshinaka F, Nakamura T. Nondestructive multiscale X-Ray tomography by combining microtomography and high-energy phase-contrast nanotomography. *Microsc Microanal*. 2018;24: 108–109.

24 Uesugi K, Hoshino M, Takeuchi A, Suzuki Y, Yagi N. Development of fast and high throughput tomography using CMOS image detector at SPring-8. *Dev X-Ray Tomogr VIII*. 2012;8506: 85060I.

25 Yoshinaka F, Nakamura T, Takaku K. Effects of vacuum environment on small fatigue crack propagation in Ti-6Al-4V. *Int J Fatigue*. 2016;91: 29–38.

26 Yoshinaka F, Xue G, Fujimura N, Nakamura T. Effect of vacuum pressure on small crack propagation in Ti-6Al-4V. *Int J Fatigue*. 2021;142: 105961.

27 Wanhill RJH. Fractography of fatigue crack propagation in 2024-T3 and 7075-16 aluminum alloys in air and vacuum. *Metall Trans A*. 1975;6: 1587–1596.

28 McEvily AJ, Velasquez G. Fatigue crack tip deformation processes as influenced by the environment. *Metall Trans A, Phys Metall Mater Sci*. 1992;23 A: 2211–2221.

29 Gach EF, Pippan R, Ravi-Chandar K, et al. Cyclic crack tip deformation - the influence of environment. *Proc 10th Int Conf Fract*. 2001.

30 Sugano M, Kanno S, Satake T. Fatigue behavior of titanium in vacuum. *Acta Metall*. 1989;37: 1811–1820.

31 Ohta A, Sasaki E. Plastic zone around fatigue cracks of pure iron in vacuum and dry air. *Acta Metall*. 1972;20: 657–660.

32 Duquette DJ, Gell M. The effect of environment on the mechanism of Stage I fatigue fracture. *Metall Trans*. 1971;2: 1325–1331.

33 Bradshaw FJ, Wheeler C. The influence of gaseous environment and fatigue frequency on the growth of fatigue cracks in some aluminum alloys. *Int J Fract Mech*. 1969;5: 255–268.

34 Lynch SP. Environmentally assisted cracking: Overview of evidence for an adsorption-induced localised-slip process. *Acta Metall*. 1988;36: 2639–2661.

35 Morris WL. The noncontinuum crack tip deformation behavior of surface microcracks. *Metall Trans A*. 1980;11: 1117–1123.

Highlights

1. Small internal cracks with local microstructure were observed using nano-CT in Ti-6Al-4V.

2. Both surface and internal small cracks in Ti-6Al-4V initiated from the alpha phase.

3. Surface cracks tips are sharper and more sensitive to external load than internal crack.

4. Internal cracks have similar crack opening behaviors to those of cracks in a vacuum.